Revelation of the effect of structural heterogeneity on microplasticity in bulk metallic-glasses

Yong Yang,[a] Jianchao Ye, and Jian Lu
The Department of Mechanical Engineering, The Hong Kong Polytechnic University, Hung Hom, Kowloon, Hong Kong, People's Republic of China

Qing Wang
The Department of Mechanical Engineering, The Hong Kong Polytechnic University, Hung Hom, Kowloon, Hong Kong, People's Republic of China; and The Institute of Materials Science, The University of Shanghai, 200072 Shanghai, People's Republic of China

Peter K. Liaw
The Department of Material Science and Engineering, The University of Tennessee, Knoxville, Tennessee 37996-2200

In this article, the shear-banding behavior in bulk metallic-glasses (BMGs) is studied using a focused ion beam (FIB)-based nanoindentation method, which involves cylindrical nanoindentation of a FIB-milled BMG microlamella and is capable of revealing the subsurface shear-band patterns down to the submicron scale. The results of the current study on a Zr-based BMG clearly show that short shear bands, with the lengths of a few hundred nanometers, could be severely kinked before growing into a longer one, which implies that structural heterogeneity plays an important role in the microplasticity of BMGs. Furthermore, through the three-dimensional finite-element simulation combined with the theoretical calculation based on the Mohr–Coulomb law, it is found that the yield strengths exhibit a large scatter as a consequence of the structural heterogeneity when microplasticity occurs in the Zr-based BMG, which is consistent with our recent findings obtained from the microcompression experiments.

I. INTRODUCTION

Bulk metallic glasses (BMGs) have been attracting a great deal of interest of materials scientists since 1960,[1] when it was first demonstrated that amorphous metals could be synthesized through the rapid quenching of supercooled liquids. In the absence of crystalline defects, such as dislocations and grain boundaries, BMGs are superior to their crystalline counterparts in yield strengths and corrosion resistance.[2,3] The unique combination of the mechanical properties of BMGs make them an excellent class of materials for a variety of applications, including sports and luxury goods, electronics, medical devices, and national defense.[4] However, this class of materials usually exhibits limited ductility at room temperature. When plasticity sets in, the lack of strain hardening gives rise to the strain localization into a few narrow shear bands within the BMGs. The subsequent catastrophic propagation of the shear bands ultimately results in the brittle-like fracture.

The inelastic deformation in BMGs originates from the existence of the atomic clusters in an amorphous structure, which can undergo shear transformations much easier than their surroundings under mechanical loadings. In the BMG literature, such atomic clusters are termed as the shear transformation zones (STZs) as an analog of dislocations in crystalline materials to initiate plastic flows in BMGs.[5] According to the unified yielding model recently developed by Johnson and Samwer,[6] the nucleation of a shear band is a strain-controlled process. When the shear strain in a BMG reaches a critical value, the shear transformations on a number of STZs percolate, leading to the formation of a shear band. If the subsequent propagation of the shear band is unhindered and driven by sufficient elastic energy release,[7] the dynamic instability in the shear band occurs, which leads to the brittle fracture.

To develop a BMG with appreciable room-temperature ductility, it is critical to understand the key mechanism that governs the shear-banding behavior. A detailed discussion on the relation between shear bands and the mechanical behavior of amorphous solids has already been provided by Schuh et al. in their recent review article and is thus skipped here. For interested readers, please refer to Ref. 8. To avoid the shear-band catastrophic propagation, a variety of nanoindentation methods, which are intended to impose constrained deformation fields on BMGs, have been used to probe the shear-banding

behaviors across a wide range of length scales.[9–23] For instance, a bonded-interface technique combined with nanoindentation was proposed to reveal the subsurface shear-banding morphologies in Vickers nanoindentation.[15,24] Such a novel indentation method has been proven useful for the study of the constitutive behavior of shear bands under a multiaxial stress state.[25] However, the lengths of the shear bands that could be clearly revealed on the cross section of the BMG sample, which consists of two separate halves glued together during Vickers nanoindentation, are a few micrometers or even longer. The deformation mechanisms at the early stage of plasticity in nanoindentation, which involves the propagation of the submicron-sized shear bands, are still elusive.

In this article, we use a nanoindentation method combined with the focused ion beam (FIB) technique to elucidate the shear-banding mechanisms at the length scale of ∼100 nm in BMGs. Like the microcompression experiments pioneered by Uchic et al.,[26] this nanoindentation method entails the integration of the classic nanoindentation approach with the FIB-based micromachining technique. It will be demonstrated that this method is capable of revealing the morphologies of shear bands of a few tens of nanometers in length underneath a cylindrical nanoindenter. The results of the current nanoindentation study provide the important experimental evidence to show that, in the microplasticity of BMGs, the structural heterogeneity plays a vital role in determining the shear-banding behavior in amorphous structures.

II. EXPERIMENTAL

A Zr-based BMG with the chemical composition of $Zr_{50}Cu_{37}Al_{10}Pd_3$ (in at.%) was selected as the model material for this study. As the first step, the surface of the 3-mm BMG disklike sample was mechanically polished to a mirror finish. Following the procedure similar to the FIB sequential-milling approach, which was established for the microcompression experiments,[26,27] the micrometer-sized lamellas were fabricated on the surface of the BMG disklike sample using FIB, as shown in Figs. 1(a) and 1(b). The thicknesses of the microlamellae ranged from ∼3 to ∼7 μm, whereas the other two dimensions were fixed at 30 and 5 μm, respectively.

During the process of the FIB micromachining, two microtrenches opposite to each other were first carved out using the high current density (∼7 nA) Ga+ ion beams at the voltage of 30 keV. The materials within the spacing between the two microtrenches served as the "precursor" of the microlamella. To reduce the tapering of the microlamella, the Ga+ ion beams with the smaller currents of 1 to 0.5 nA were used sequentially to smooth out the side surfaces of the microlamella. The final step of the FIB treatment was to trim the side surface with the 100-pA ion beam to minimize the FIB-induced damage.
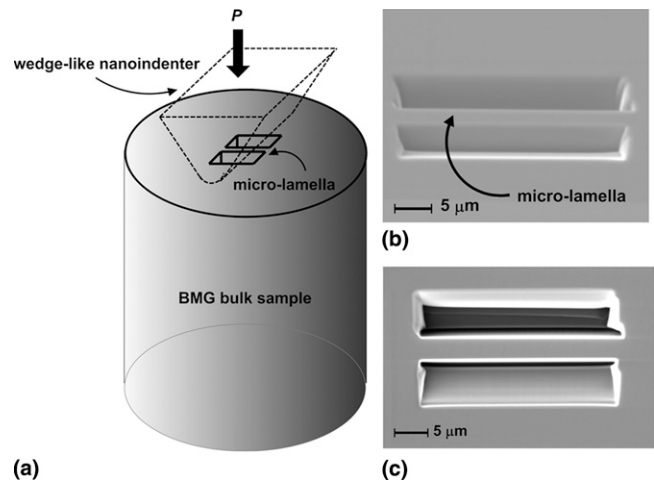
FIG. 1. (a) Sketch of the microlamella fabricated on the top surface of an BMG disklike bulk sample, which is subsequently compressed by a wedgelike nanoindenter (note that the sketch is not to scale); (b) 52° angle view and (c) plan view of the Zr-based BMG microlamella fabricated using FIB.

After the tedious FIB micromachining, it was evident that both side surfaces of the microlamella were almost perpendicular to the top surface of the BMG disk [Fig. 1(b)].

For the nanoindentation experiment, the BMG disklike sample was attached onto a custom made sample holder, which enabled the fine tuning of the sample orientation in the three angular directions with the accuracy of ∼1°. A custom made wedgelike diamond nanoindenter, which was 10 μm long and had a 60° half-included angle and 1-μm tip radius, was incorporated into the Hysitron Triboscratch nanoindentation system (Minneapolis, MN) for the indentation of the BMG microlamella [Fig. 1(c)]. It should be emphasized here that, prior to the nanoindentation experiments, the sample tilting was examined by making two crossed indentation marks on the sample surface with the wedgelike nanoindenter. Since the indentation impressions were made with the same loads, severe sample tilting could be inferred if one mark was longer than the other. After the examination and calibration of the sample alignments, the indentation experiments were finally conducted at the fixed displacement rate of 25 nm/s and the maximum penetration depths were controlled less than 500 nm to ensure the deformation fields were conformable to a cylindrical indentation.

III. RESULTS AND ANALYSES

A. Experimental load versus displacement curves

Figures 2(a) and 2(b) present the deformation morphologies of the indented microlamellae at the indentation depths of 300 nm [Fig. 2(a)] and 200 nm [Fig. 2(b)], respectively. It is evident that the number of shear bands, emerging on both the side and top surfaces of the microlamella, accumulate to one side of the indent, leaving the
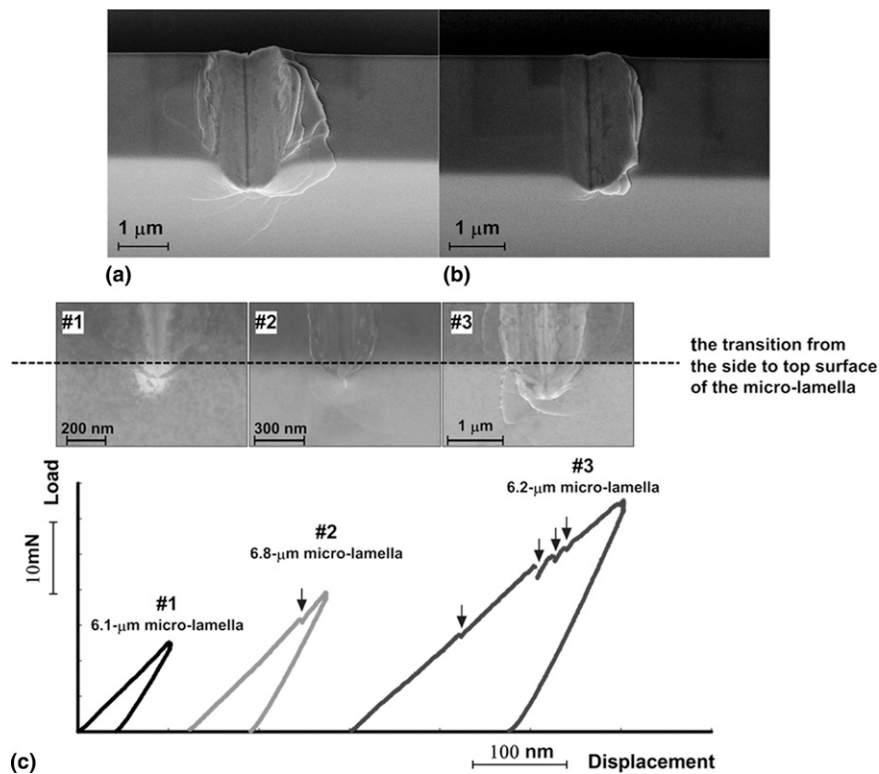
FIG. 2. Perspective views of the (a) deep and (b) shallow indents made on the microlamella samples; and (c) comparison of the load–displacement curves obtained from three different BMG microlamellae (note that the load–displacement curves are numbered in accord with the high-resolution micrographs shown above and the arrows indicate the significant load drops).

other side less populated by the shear bands. Such an asymmetrical shear-banding pattern was also reported in the other nanoindentation experiments,[14] which implied that BMGs may possess a certain degree of structural heterogeneity at the submicron scale despite their overall structural homogeneity at the macroscopic scale.

The typical experimental load–displacement curves for three different indentation depths are shown in Fig. 2(c), above which the corresponding high-resolution scanning electron microscopy (HRSEM) images of the subsurface shear-banding morphologies are displayed. Since our high load Hysitron nanoindentation system has a displacement resolution of ~2 nm and a load resolution of ~50 μN, any discontinuity in the mechanical response caused by the underlying shear-banding process can hardly be detected below those two mechanical limits of the testing machine. Evidently, the first detectable load drops in the nanoindentation experiments do not correspond to the yielding of the BMG microlamella. From the load–displacement curve, it can be seen that plasticity occurred in an apparently smooth manner prior to the appearance of the load serrations. Physically, the smoothness of the loading curve at the elastoplastic transition point may be attributed to the mechanical confinement on the newly borne shear band from its elastic surroundings. It should be emphasized here that we didn't find any traces of submicron-sized shear bands emerging on the side surface of the

microlamella underneath the indenter at the elastoplastic transition point. The first submicron-sized shear band appeared on the side surface in accordance with the first load drop.

As the indentation depth was increased, more load drops were observed on the corresponding load–displacement curve. Accordingly, the number of the subsurface shear bands increased. However, the number of the load drops does not have a one-to-one correspondence with that of the subsurface shear bands. Instead, the latter is usually higher than the former, indicating that one single load drop may be caused by multiple shear-band operations.

B. Elastic stress states in BMG microlamellae

To ascertain the elastoplastic transition point in this study, the three-dimensional (3D) finite-element (FE) simulation was performed to simulate the elastic load–displacement curve of the microlamella. Because of symmetry, only half of the sample geometry needs to be built into the FE model, whose boundary conditions are sketched in Fig. 3(a). It should be noted that the material is modeled as elastic at the current stage. To simplify our analysis, the nanoindenter was assumed as a rigid body with a frictionless contact. To optimize the computational cost and accuracy, the mesh size was refined around the contract area, whereas coarsened in the volumes far away
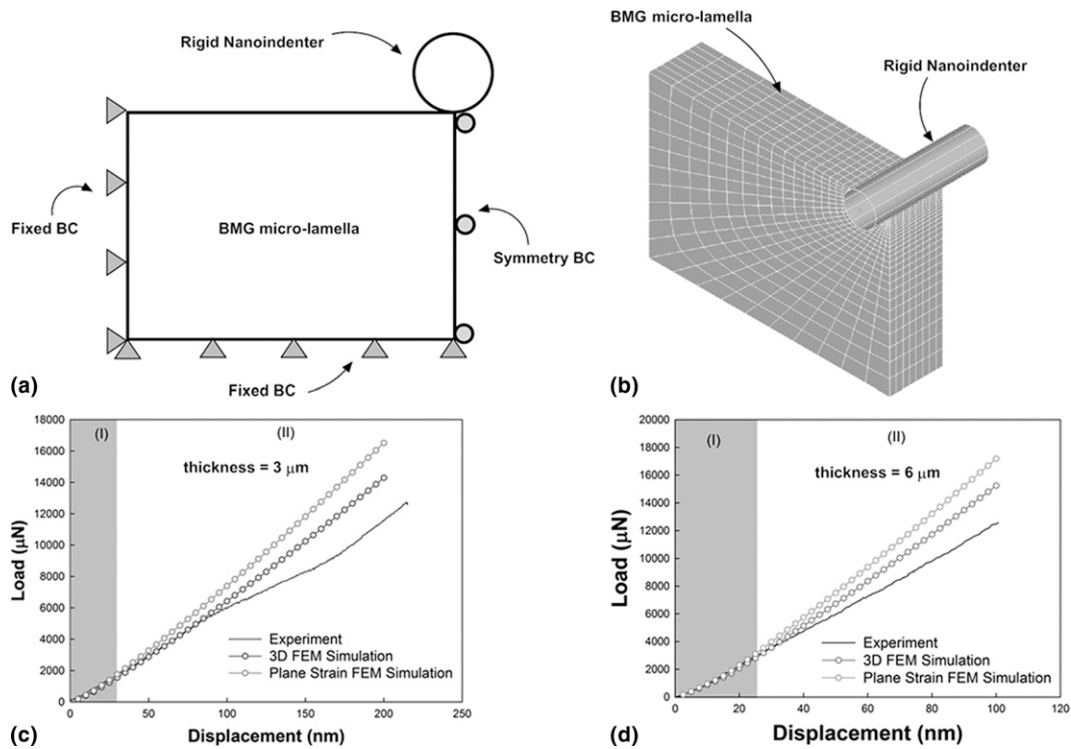
FIG. 3. (a) Sketch of the boundary conditions (BCs) applied to the 3D FE model; (b) the meshed 3D FE model of the microlamella; the comparison of the loading curves obtained from the experiment, the 3D FE simulation and the 2D plane-strain FE simulation for the (c) 3-μm microlamella and (d) 6-μm microlamella (note that Region I and II correspond to the dominant stress states of the plane strain and mixed type within the microlamella, respectively).

from the contact [Fig. 3(b)]. During the simulation, the model size and mesh density were checked to ensure that the computational results were insensitive to the boundary conditions and mesh size. For the current Zr-based BMG, the Young's modulus and Poisson's ratio were taken as ∼100 GPa and ∼0.366, respectively.[27]

Figures 3(c) and 3(d) show the experimental loading curves, obtained from the 3- and 6-μm-thick BMG microlamellae, respectively, in comparison with the 3D and two-dimensional (2D) plane-strain FE simulation results. It can be seen that all the curves overlap at the small displacements. For the 3-μm BMG microlamella, the agreement between the experiments and 3D FE simulations is seen throughout the whole elastic regime. The deviation of the experimental data from the 3D FE simulation results thus determines the elastoplastic transition point. However, the divergence of the 2D FE simulation results from the 3D ones takes place before the elastoplastic transition occurs, suggesting that the dominant stress state is essentially of a 3D type at the onset of plasticity in the 3-μm-thick microlamella. In contrast, both 2D and 3D FE simulation results override each other almost in the whole elastic deformation regime for the 6-μm microlamella. The elastoplastic transition manifests itself as the deviation of the experimental data from either the 3D or the 2D FE simulation results. This

trend implies that, as the thickness of the microlamella expands, the dominant stress state at the onset of plasticity tends to change from a 3D stress state to a 2D plane-strain stress state.

C. Estimation of yield strengths of BMG microlamellae

On the basis of the previous findings, a simplified numerical scheme is proposed as follows to estimate the yield strength of the BMG microlamella. It is well known in the field of BMGs that the plasticity of BMGs obeys the Mohr–Coulomb's law.[28–31] On the potential shear plane, the following equation must be satisfied to trigger a yielding process:

$$\tau_0 = |\tau_n| + \alpha\sigma_n \quad , \qquad (1)$$

where τ_0 is the intrinsic shear strength; τ_n and σ_n denote the shear and normal stress acting on the shear plane with a unit normal of n, respectively; and α is the normal stress coefficient of a BMG.

In uniaxial compression experiments, as shown in Fig. 4(a), it can be easily derived that the angle of the potential shear plane, θ, relative to the loading axis is related to the normal stress coefficient, α, as follows[28]:

$$\alpha = 1/\tan(2\theta) \quad . \qquad (2)$$
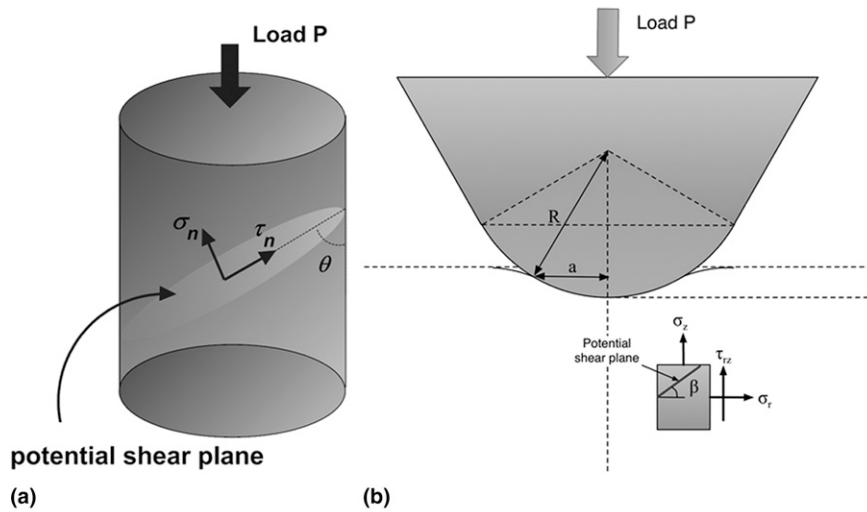
FIG. 4. Symbols used in the derivation of the BMG yield strength in (a) normal compression of an BMG cylinder and (b) cylindrical nanoindentation of an BMG microlamella.

For the current Zr-based BMG, the shear angle θ observed in the normal compression experiments is around $42°$ and, thus, the normal stress coefficient, α, is ~ 0.105.[32]

For the present cylindrical nanoindentation experiments, the stress state is much more complicated than that in the uniaxial experiments. To simplify our analysis, the stress state of a plane strain type is used to estimate the yield strength of the microlamella. It should be pointed out that this approximation is valid only for the thick microlamellae, for which the plane-strain stress state has been proven dominating the sample's elastic deformation behavior. In such a case, the right side of Eq. (1) can be expanded as

$$\tau_{eff} = \left| \sin\beta\cos\beta(\sigma_r - \sigma_z) + \tau_{rz}(\cos^2\beta - \sin^2\beta) \right|$$
$$+ \alpha\left(\sin^2\beta\sigma_r + \cos^2\beta\sigma_z + 2\sin\beta\cos\beta\tau_{rz}\right) \quad , \quad (3)$$

in which the three Hertizian stress components σ_r, σ_z, and τ_{rz} are defined in Fig. 4(b); β denotes the angle of the potential shear plane relative to the horizontal axis and the effective stress, τ_{eff}, can be viewed as an analog of the measure of the von Mises stress for the yielding of a crystalline material.

According to the Mohr–Coulomb law, shear banding tends to occur in the BMG microlamella on the shear plane with the maximum τ_{eff}. To assess the global maximum of τ_{eff} in the plane-strain stress field, the local maximum of τ_{eff} was first sought numerically for each material point underneath the indenter by substituting the expressions of the three Hertizian stress components into Eq. (3) (see the Appendix for details).

Figures 5(a) and 5(b) present the contour plots of the point-wise maximum of τ_{eff} normalized by P_0 at $\alpha = 0$ and 0.105, respectively. Here, P_0 is the average pressure

defined in the Appendix. Evidently, the shear-band nucleation site deepens along the axis of symmetry as the α value increases. For completeness, the global maximum of τ_{eff}, as normalized by P_0, and the depth of the shear-band nucleation site z_m, as normalized by the contact radius a, are plotted in Fig. 5(c) against different values of α. The ascending trend of z_m/a versus α is consistent with our previous observations from Figs. 5(a) and 5(b). Accordingly, the ratio of the global maximum of τ_{eff}, to P_0 decreases. When $\alpha = 0$, the classic Hertzian solution, i.e., the global maximum of $\tau_{eff} = 0.3P_0@ z_m = 0.787a$, is recovered.[33]

The extracted shear strengths, τ_0, of the Zr-based BMG from the cylindrical nanoindentation experiments are plotted in Figs. 5(c) and 5(d). It can be seen that the experimental data follow a normal distribution and are scattered in the range from ~ 0.85 to ~ 1.3 GPa. The averaged shear strength of the Zr-based BMG is around ~ 1.1 GPa and $\sim 3\%$ of the corresponding shear modulus (~ 36.6 GPa). In the normal compression experiments, the yield strength of the Zr-based BMG was measured to be around $\sim 1.9 \pm 0.1$ GPa[32] and the corresponding shear strength was ~ 0.9 GPa on average, which is close to the tail value of ~ 0.85 GPa of the present nano-indentation measurements but about 20% lower than the average value of ~ 1.1 GPa.

D. Subsurface shear-band patterns at the submicron scale

In the previous indentation studies of BMGs, the experimental revelation of the subsurface shear-band structures has been attempted using different approaches,[12,14,18,34,35] which entails the Vickers indentation on a bonded interface[14] or the wedge indentation on a thick BMG
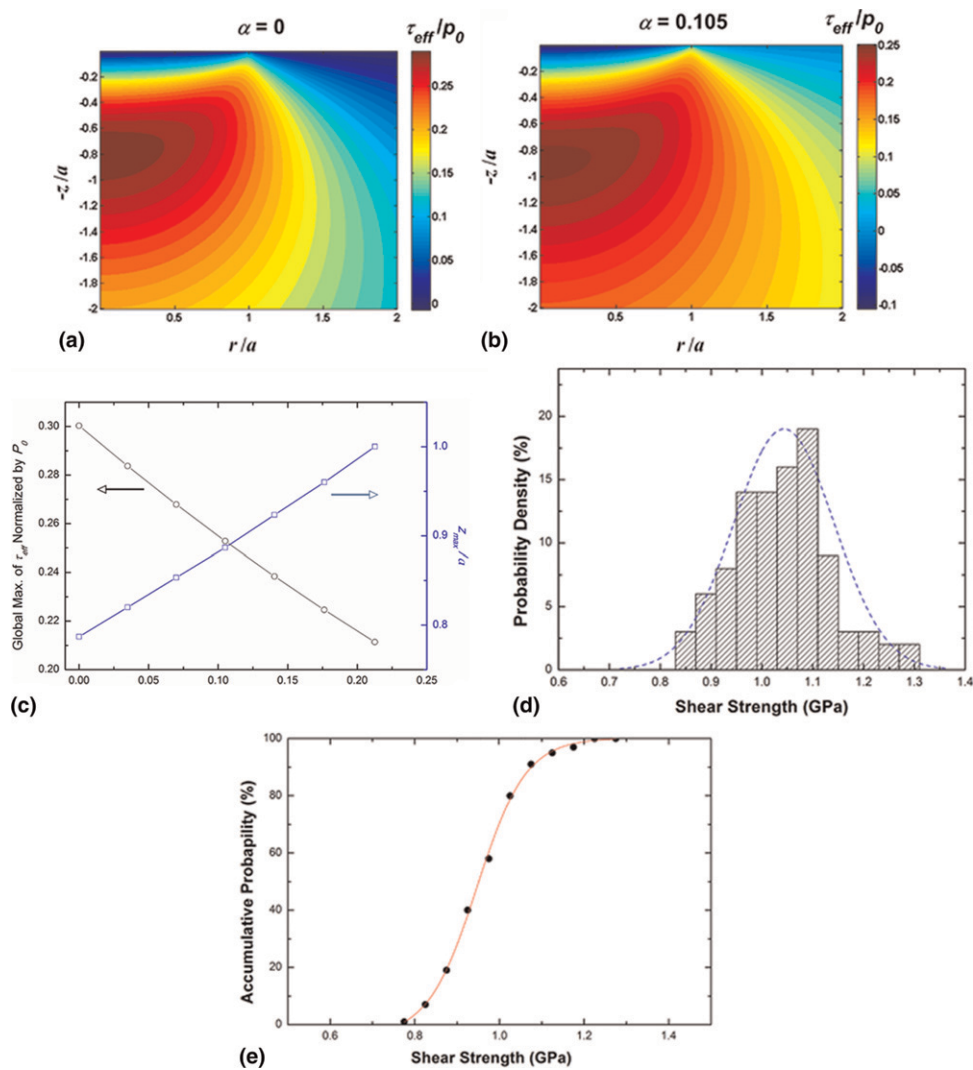
FIG. 5. Contour plots of the local maximum of τ_{eff} normalized by P_0 at (a) $\alpha = 0$ and (b) $\alpha = 0.105$; (c) variations of the normalized global maximum of τ_{eff} and the depth of the shear-band nucleation site with the increasing α; the distributions of (d) probability density and (e) accumulated probability of the measured shear strengths of the Zr-based BMG. (color online)

plate.[12,18,34] Based on the experimental results, it was found that the pattern of the shear bands exposed on the surface of observation generally matched the predictions of the continuum theories well at the macroscopic scale.[16,18,34] However, it is not clear at this time if such a pattern match can be extended to the submicron scale.

For the sake of comparison, an elastoplastic FE model, incorporating a homogeneous and isotropic material that follows the pressure sensitive Drucker–Prager yield criterion,[36] was built into the commercial package ANSYS (Canonsburg, PA) to mimic the deformation behavior of BMGs. A similar model of a continuum type was used by Vaidyanathan et al.[28] to fit the load–displacement curves that were obtained in the indentation study of a Zr-based BMG. To reduce the computational cost, a 2D plane strain instead of a 3D elastoplastic FE simulation was performed since the out-of-plane deformation, which is caused by the 3D stress state, is not the focus of our current study. Furthermore, it should be emphasized that the elastoplastic FE simulation was not intended to fit the experimental data since the constitutive behavior of BMGs is not of a continuum type at the submicron scale. The purpose of the elastoplastic simulation is to highlight the difference in the shear-band patterns between the material with the ideal mechanical homogeneity and isotropy and the real Zr-based BMG. In other words, the FE model in our current study serves as a model material possessing no structural heterogeneity.
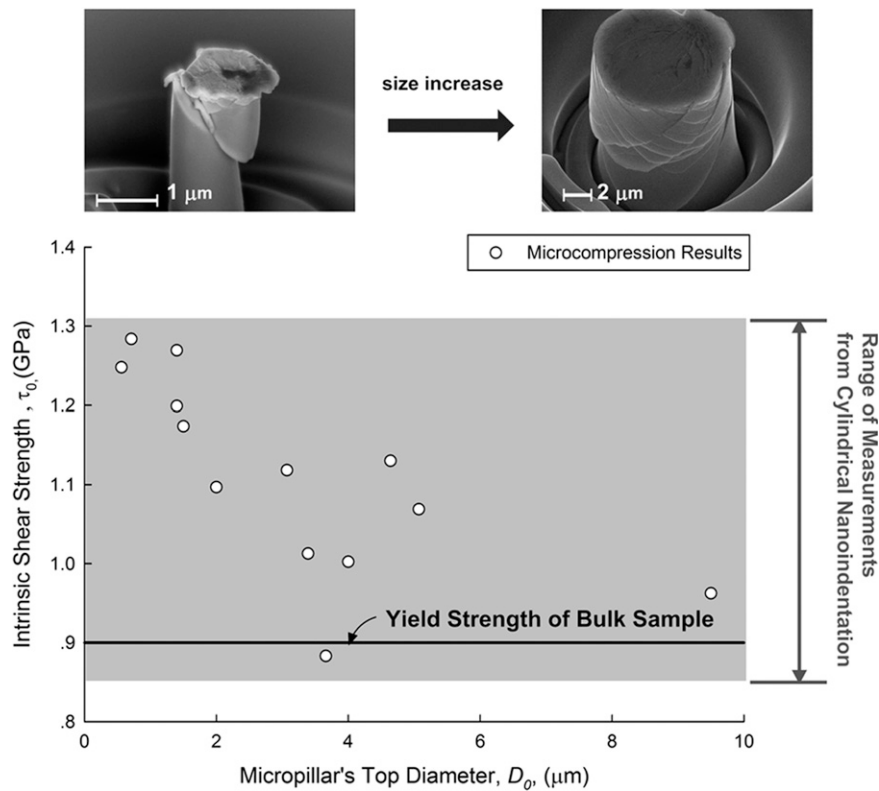
FIG. 6. Variation in the intrinsic shear strengths extracted from microcompression experiments (the insets demonstrate the persistence of the shear-banding deformation mode in the micropillars with the initial diameters ranging from ~500 nm to ~10 μm).

According to Su et al.,[18] subsurface shear-band trajectories can be captured numerically with the von Mises plastic strains at the macroscopic scale. In our FE simulations, the same approach was adopted and the shear bands in the FE simulations were, thus, revealed using the von Mises plastic strains. As shown in Figs. 6(a)–6(c), the plastic strains are initially distributed in a half-circular region underneath the indenter [Fig. 6(a)]; as the indentation depth increases, the plastic strains are concentrated into two narrow bands in the radial directions [Fig. 6(b)], reminiscent of the formation of a V-shaped shear-band pair as observed in the macroscopic wedge indentation experiments.[16,18,34] With the further increase in the indentation depth, the shear bands cross each other at the axis of symmetry and a new V-shaped shear-band pair appears above the crossing shear bands [Fig. 6(c)].

In contrast, only a single shear band in the radial direction was observed in the cylindrical nanoindentation experiment at $h = 150$ nm [Fig. 6(d)], which corresponded to a single load drop on the corresponding load–displacement curve. As the indentation depth was increased to 200 and 450 nm, the V-shaped shear-band pairs and crossing shear bands were observed underneath the indenter, respectively, which indicates that the experimental observations are indeed similar to what the FE simulations predict in the general trend in some cases. However, one of the shear bands in Fig. 6(d) was heavily kinked, which differs from the FE simulation results. Interestingly, a 100-nm shear-band embryo was observed below the two crossing shear bands in Fig. 6(e), which indicates that shear banding still prevails down to the length scale of ~100 nm for the current Zr-based BMG.

Kinking of shear bands was widely observed as the subsurface radial shear bands extended to a few micrometers in size. As shown in Figs. 7(a)–7(d), shear bands were propagating along the tortuous trajectories. The kinks along the shear bands had the spacing of a few hundreds of nanometers and displayed the kink angles ranging from ~18° to ~40°. Despite the kinks, it can be seen that the overall trends of the radial shear-band trajectories roughly follow the predictions of the FE simulations in their directions [Fig. 7(e)]. However, almost all the radial shear bands are unpaired, accumulating to one side of the indent. As compared with the FE simulation results for an ideally homogeneous and isotropic material, one-half of the shear bands seem missing. It should be noted that such an asymmetrical shear-banding pattern was qualitatively captured by the recent molecular dynamics (MD) simulations,[17,37] into which the structural variation in amorphous metals, such as the short range order (SRO), was incorporated.

J. Mater. Res., Vol. 25, No. 3, Mar 2010

569
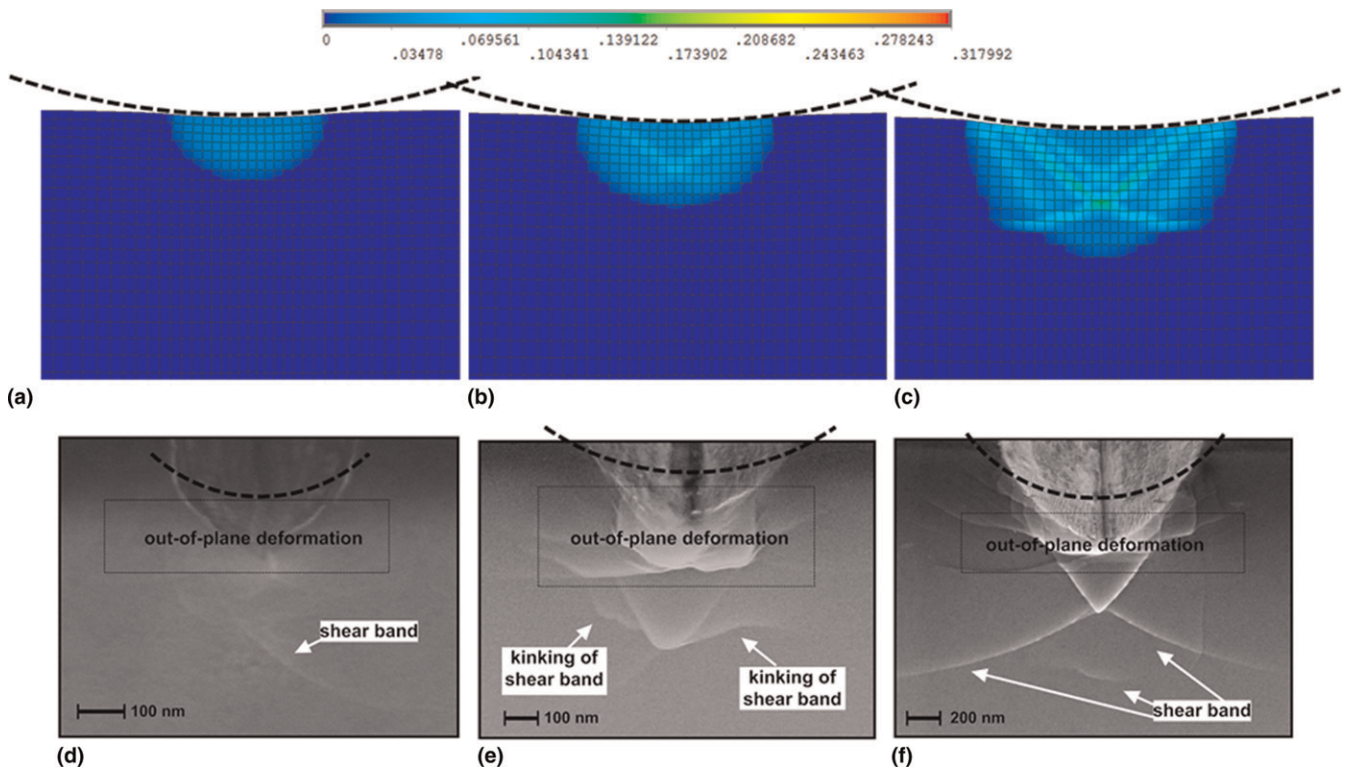
FIG. 7. (a)–(c) Evolution of the von Mises plastic strain under a cylindrical indenter in an ideally homogeneous and isotropic material obeying the pressure sensitive yield criterion (Drucker–Prager model) with the increasing indent depths (results obtained from the plane-strain FE simulations); the high-resolution micrographs showing the 45° angle views of the subsurface shear-band structures at (d) h = 150 nm, (e) h = 200 nm, and (f) h = 450 nm (h = the indent depth). (color online)

However, the heavy kinking of the shear bands was not reported even with the MD simulations.

IV. DISCUSSION

A. Variation of BMG yield strengths at the submicron scale

In the BMG literature, the size effect on yield strengths is still an issue under debate.[38] Other than the nano-indentation experiments,[9,10] the microcompression experiments have also been used to extract the BMG yield strengths.[38–43] In the microcompression studies, the size effect was investigated by varying the diameters of the BMG micropillars. However, conflicting results have been reported by different research groups. It is noted that the discrepancy originated mainly from the way of measuring the yield strengths of the BMG micropillars. For instance, no size effect was discernable if the micropillar's yield strength was interpreted as the average stress on the cross section of a micropillar at the middle height[41]; however, a pronounced size effect was found if the average stress on the top surface of a micropillar was used.[42,43] As mentioned in Ref. 41, the use of an average stress on a certain cross section cannot be taken as a rigorous measure of the yield strength because of the stress nonuniformity in the micropillars. A detailed stress analysis is required to

understand how the geometry of a micropillar affects the initiation of a shear band.

Recently, the shear-plane criterion proposed by Packard and Schuh[9] was used to study the geometry effect of a micropillar on the initiation and propagation of a shear band by Ye et al.[32] Through the rigorous analysis, it was shown that the yield strength of a BMG micropillar could be extracted accurately after calibrating the effects arising from the pillar tapering and shear-band nucleation site. Based on the micropillar yielding model developed in Ref. 32, microcompression experiments were conducted on the current Zr-based BMG and the intrinsic shear strengths of the micropillars were measured as a function of the top diameters of the micropillars.

As shown in Fig. 8, the measured shear strengths of the micropillars are distributed within the range from ~0.88 to ~1.3 GPa. Such a data scatter agrees well with that observed in the present cylindrical nanoindentation experiments. Given the current understanding of the shear-banding process in BMGs,[39,43] it is believed that, unlike dislocations in crystalline structures, shear bands do not possess an intrinsic strengthening mechanism by interacting with each other in amorphous structures. The size effect arising from the sample size reduction is, therefore, a manifestation of the Weibull size effect. In such a case, if the statistic variation of the yield
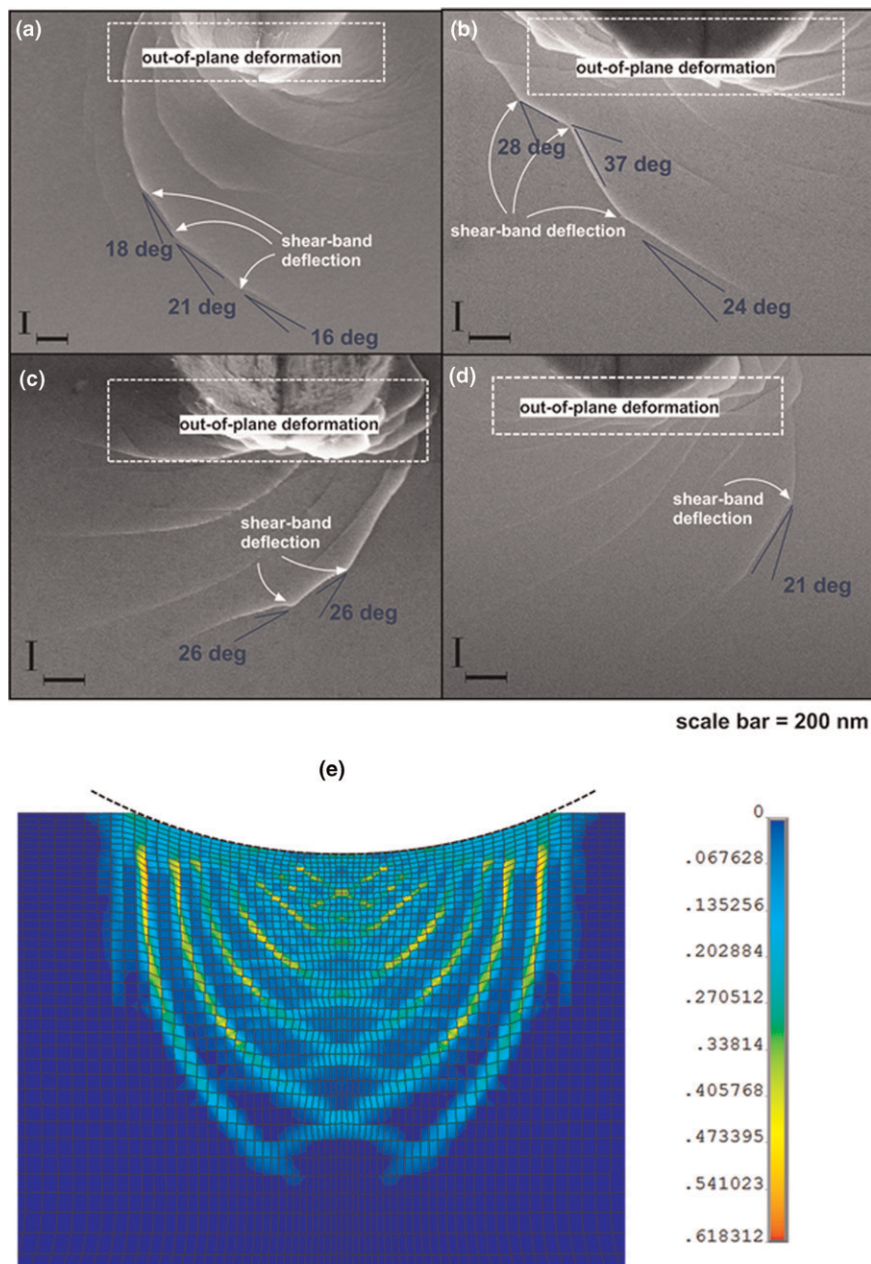
FIG. 8. (a)–(d) Micrographs of the underlying shear-band morphologies at $h = 500$ nm; (e) distribution of the von Mises plastic strain under a cylindrical indenter in an ideally homogeneous and isotropic material obeying the pressure sensitive yield criterion (Drucker–Prager model) at severe plastic deformation (results obtained from the plane-strain FE simulations). (color online)

strengths of the current Zr-based BMG was sampled by the present cylindrical nanoindentation experiments, the experimental results should be consistent with those obtained from the microcompression experiments as long as enough data points were collected, which is just the case as already seen in Fig. 8. Furthermore, it is worthwhile mentioning that the inhomogeneous deformation mode persisted in the micropillars across the length scale from ~500 nm to ~10 μm and there was no transition from the shear-band mediated to homogeneous deformation mode observed (the insets of Fig. 8), which is also

consistent with our observations from the cylindrical nanoindentation experiments.

B. Origin of shear-band kinking at the submicron scale

Evidently, the shear-band kinking implies that the investigated Zr-based BMG is not really "homogeneous" at the submicron scale as usually anticipated for amorphous structures. As proposed by Harmon et al.,[44] the elastoplastic transition in BMGs is triggered by the breakdown of the elastic confinement surrounding a

STZ. The percolation of the shear transformation events occurring on the individual STZs then leads to the formation of a shear band. Based on the STZ model, one possible explanation for the kinked shear band can be
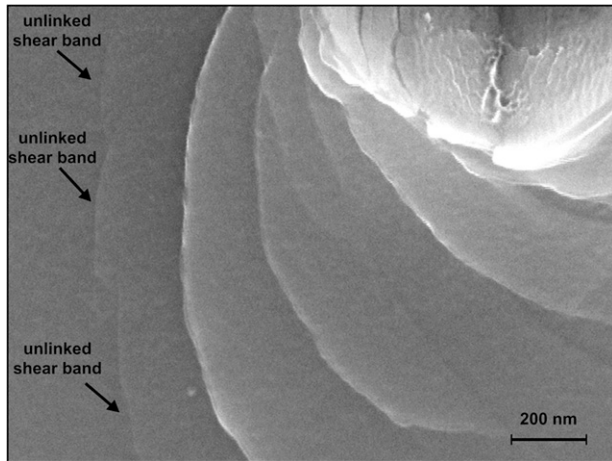
FIG. 9. HRSEM micrograph showing the unlinked shear bands lined up along the shear trajectory similar to those with shear-band kinks.

proposed, i.e., the short shear bands nucleate by linking up the regions of high concentrations of STZs and the spatial heterogeneity of such regions results in the shear-band kinking. Careful examination of the shear-banding morphology in the regions far away from the mechanical contact, where the effective strain may just suffice to cause the nucleation of the individual shear bands but yet to link them up, did show the unlinked shear bands (Fig. 9). Obviously, these shear bands appear to be somewhat lined up along a shear trajectory similar to those seen to its right but display an offset of about a few tens of nanometers in the horizontal direction. The unlinked shear bands, together with the observed shear-band kinking; strongly imply that the linking of the short shear bands is a plausible mechanism for the shear-band extension in the microplasticity of the Zr-based BMG.

On the other hand, the shear-band kinking could also result from the nanocrystallination induced by the propagation of the shear band.[45–47] For instance, wavy shear bands, which had an average wavelength of $\sim$100 nm, were revealed in the CuZr metallic glass by Hajlaoui et al.[47] through their in situ deformation transmission
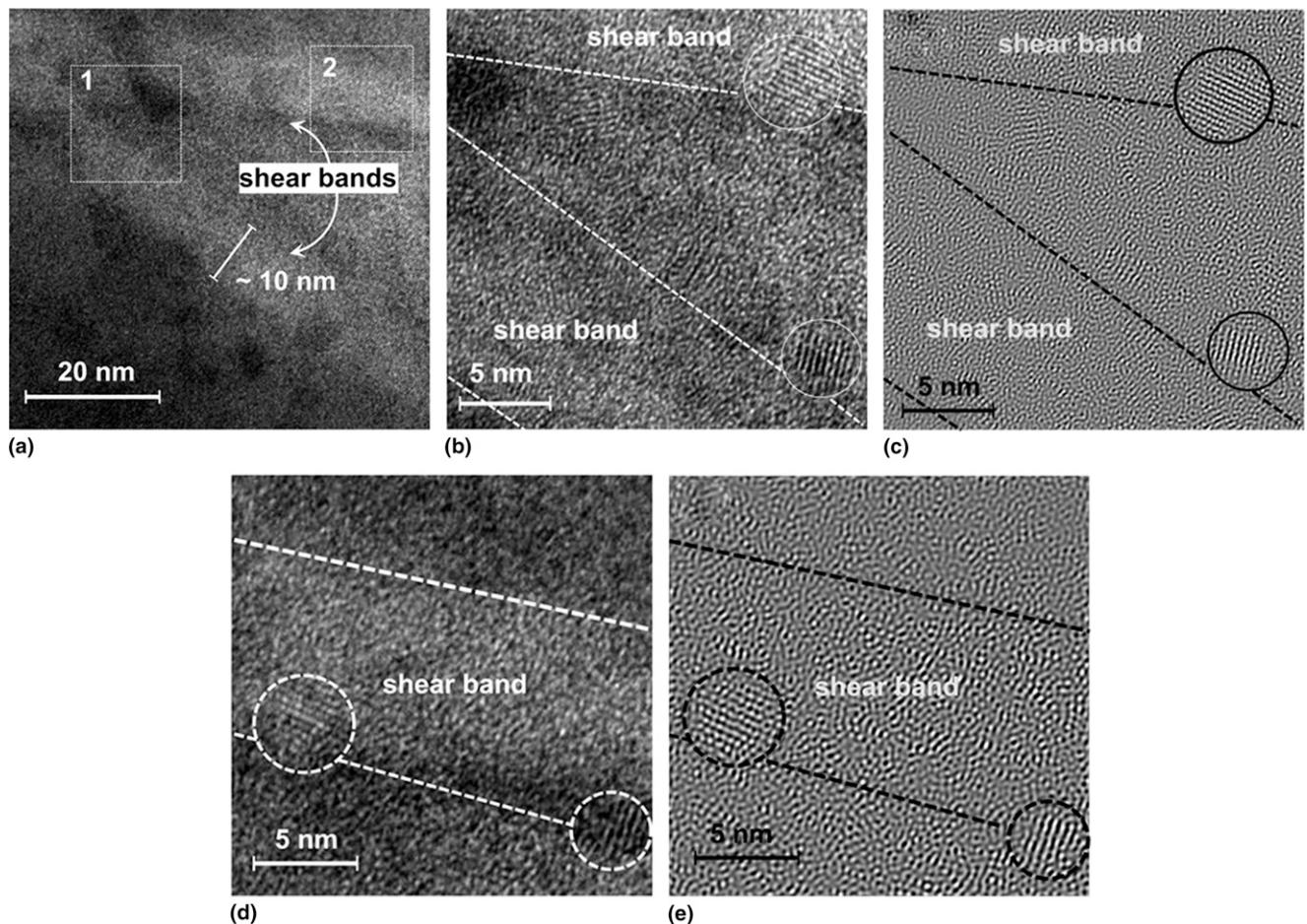
FIG. 10. (a) TEM image of two 10-nm-thick shear bands found in the area close to a shear-band kink; (b) high-resolution TEM image of Region 1 in (a); (c) fast Fourier transformation (FFT) filtered image of (b); (d) high-resolution TEM image of Region 2 in (a); and (e) the FFT filtered image of (d) (note that the circled regions correspond to the nanocrystals).

electron microscopy (TEM) analysis. Within these wavy shear bands, nanocrystals were observed growing together with a tortuous shear crack. To ascertain the origin of the shear-band kinking observed in the cylindrical nanoindentation experiments, multiple TEM thin foils were cut from the microlamella samples using FIB. Prior to the TEM examination, the TEM thin foils were thinned down to a thickness of less than ~50 nm for the revelation of the shear bands at the atomistic scale. As shown in Fig. 10(a), two 10-nm-thick shear bands were observed on one of the TEM thin foils. Along these shear bands, a few nanocrystals, which had an average size of ~5 nm, were found residing along the shear-band boundaries [Figs. 10(b)–10(e)]. It should be mentioned that the shear-band boundaries were sketched with the dashed lines in Figs. 10(b)–10(e) based on the contrast shown in the low-resolution TEM image of the shear bands [Fig. 10(a)].

Despite the nanocrystallization seen along the shear bands, the shear-band profiles still remain as straight locally. It is noted that the reported shear-band waviness mainly occurred on the shear bands already expanded from a thickness of ~10 to ~100 nm. Since the shear-band thickening came along with the nanocrystal growth and shear-band cracking,[47] the alteration of the shear-band profile caused by the nanocrystallization is likely to occur in the severely deformed BMGs, whose status is almost close to the final stage of failure. For the current BMG microlamellae, the observed shear-band kinking is unlikely to be caused by the 5-nm sized nanocrystals. In the meantime, it is worthwhile mentioning that the nucleation of nanocrystals was confined to the shear bands as observed in the TEM thin foil, which means that the observed nanocrystallization was induced by the shear-banding process rather than by the ion-beam bombardment during the TEM sample preparation process.[48]

According to Shimitz et al.,[49,50] the stress singularity ahead of the shear-band tip scales with $\sqrt{l/w}$, where l and w denote, respectively, the shear-band length and width. Therefore, for long shear bands, such as those observed in the mm-sized specimens, the stress singularity at the shear-band tip is sufficient to break through any obstacles ahead of the shear band. In such a case, the shear trajectories are determined by the indentation stress field and the kinking of shear bands is, thus, smeared out by the overall smoothness of the shear trajectories. In contrast, the microscale shear trajectories are more structurally sensitive and affected by the stress state as well as the structural heterogeneity existing in amorphous structures.

V. CONCLUSIONS

In summary, a FIB-based nanoindentation method is used in this article to study the plastic deformation mechanism in BMGs. Using the current method, the intrinsic shear strength of the Zr-based BMG was estimated, which clearly showed a size effect on the BMG yield strengths and was consistent with the microcompression results. At the submicron/micrometer scale, it was found that kinking of shear bands became ubiquitous as opposed to the smooth shear trajectories observed at the macroscopic scale. Such a shear-band kinking phenomenon provides important experimental evidence to demonstrate the impact of structural heterogeneity on the plastic deformation in BMGs at the early stage.

REFERENCES

1. K. Klement, R.H. Willens, and P. Duwez: Non-crystalline structure in solidified gold-silicon alloys. *Nature* **187,** 869 (1960).
2. A.L. Greer: Metallic glasses. *Science* **267,** 1947 (1995).
3. M.F. Ashby and A.L. Greer: Metallic glasses as structural materials. *Scr. Mater.* **54,** 321 (2006).
4. M. Telford: The case for bulk metallic glass. *Mater. Today* **7,** 36 (2004).
5. A.S. Argon: Plastic deformation in metallic glasses. *Acta Metall.* **27,** 47 (1979).
6. W.L. Johnson and K. Samwer: A universal criterion for plastic yielding of metallic glasses with a $(T/T_g)^{2/3}$ temperature depedence. *Phys. Rev. Lett.* **95,** 195501 (2005).
7. J.C. Ye, J. Lu, Y. Yang, and P.K. Liaw: Study of the intrinsic ductile to brittle transition mechanism of metallic glasses. *Acta Mater.* **57,** 6037 (2009).
8. C.A. Schuh, T.C. Hufnagel, and U. Ramamurty: Mechanical behavior of amorphous alloys. *Acta Mater.* **55,** 4067 (2007).
9. C.E. Packard and C. Schuh: Initiation of shear bands near a stress concentration in metallic glass. *Acta Mater.* **55,** 5348 (2007).
10. H. Bei, Z.P. Lu, and E.P. George: Theoretical strength and the onset of plasticity in bulk metallic glasses investigated by nanoindentation with a spherical indenter. *Phys. Rev. Lett.* **93**(12), 125504 (2004).
11. C.A. Schuh, A.C. Lund, and T.G. Nieh: New regime of homogeneous flow in the deformation map of metallic glasses: Elevated temperature nanoindentation experiments and mechanistic modeling. *Acta Mater.* **52,** 5879 (2004).
12. A. Antoniou, A.F. Bastawros, C.C.H. Lo, and S.B. Biner: Deformation behavior of a zirconium based metallic glass during cylindrical indentation: In situ observations. *Mater. Sci. Eng., A* **394,** 96 (2005).
13. M.J. Kramer, D.J. Sordelet, A.F. Bastarows, and X. Tan: Absence of crystallization during cylindrical indentation of a Zr-based metallic glass. *J. Non-Cryst. Solids* **351,** 2159 (2005).
14. U. Ramamurty, S. Jana, Y. Kawamura, and K. Chattopadhyay: Hardness and plastic deformation in a bulk metallic glass. *Acta Mater.* **53,** 705 (2005).

15. H.W. Zhang, X.N. Jing, G. Subhash, L.J. Kecskes, and R.J. Dowding: Spatiotemporally inhomogeneous plastic flow of a bulk-metallic glass. Investigation of shear band evolution in amorphous alloys beneath a Vickers indentation. *Acta Mater.* **53**(14), 3849 (2005).

16. A. Antoniou, A. Bastawros, and B. Biner: Experimental observations of deformation behavior of bulk metallic glasses during wedge-like cyclindrical indentation. *J. Mater. Res.* **22**(2), 514 (2007).

17. Y. Shi and M.L. Falk: Does metallic glass have a backbone? The role of percolating short range order in strength and failure. *Scr. Mater.* **54**, 381 (2006).

18. C. Su and L. Anand: Plane strain indentation of a Zr-based metallic glass: Experiments and numerical simulation. *Acta Mater.* **54**(1), 179 (2006).

19. N. Li, L. Liu, Q. Chen, J. Pan, and K.C. Chan: The effect of free volume on the deformation behaviour of a Zr-based metallic glass under nanoindentation. *J. Phys. D: Appl. Phys.* **40**, 6055 (2007).

20. F. Yang, K. Geng, P.K. Liaw, G. Fan, and H. Choo: Deformation in a $Zr_{57}Ti_5Cu_{20}Ni_8Al_{10}$ bulk metallic glass during nanoindentation. *Acta Mater.* **55**, 321 (2007).

21. W. Jiang, G.J. Fan, F. Liu, G.Y. Wang, H. Choo, and P.K. Liaw: Spatiotemporally inhomogeneous plastic flow of a bulk-metallic glass. *Int. J. Plast.* **24**(1), 1 (2008).

22. Y.C. Lu, S.N.V.R.K. Kurapati, and F. Yang: Finite element analysis of cylindrical indentation for determining plastic properties of materials in small volumes. *J. Phys. D: Appl. Phys.* **41**(11), 115415 (2008).

23. D. Pan, A. Inoue, T. Sakurai, and M.W. Chen: Experimental characterization of shear transformation zones for plastic flow of bulk metallic glasses. *Proc. Nat. Acad. Sci. U.S.A.* **105**(39), 14769 (2008).

24. W. Jiang, G.J. Fan, F. Liu, G.Y. Wang, H. Choo, and P. Liaw: Spatiotemporally inhomogeneous plastic flow of a bulk-metallic glass. *Int. J. Plast.* **24**, 1 (2008).

25. H. Zhang, S. Maiti, and G. Subhash: Evolution of shear bands in bulk metallic glasses under dynamic loading. *J. Mech. Phys. Solids* **56**(6), 2171 (2008).

26. M. Uchic, D.M. Dimiduk, J.N. Florando, and W.D. Nix: Sample dimensions influence strength and crystal plasticity. *Science* **305**, 986 (2004).

27. Y. Yang, J.C. Ye, J. Lu, F.X. Liu, and P.K. Liaw: Effects of specimen geometry and base material on the mechanical behavior of focused-ion-beam-fabricated metallic-glass micropillars. *Acta Mater.* **57**, 1613 (2009).

28. R. Vaidyanathan, M. Dao, G. Ravichandran, and S. Suresh: Study of mechanical deformation in bulk metallic glass through instrumented indentation. *Acta Mater.* **49**, 3781 (2001).

29. C.A. Schuh and A.C. Lund: Atomistic basis for the plastic yield criterion of metallic glass. *Nat. Mater.* **2**, 449 (2003).

30. M.N.M. Patnaik, R. Narasimhan, and U. Ramamurty: Spherical indentation response of metallic glasses. *Acta Mater.* **52**(11), 3335 (2004).

31. A. Dubach, K.E. Prasad, R. Raghavan, J.F. Loffler, J. Michler, and U. Ramamurty: Free-volume dependent pressure sensitivity of Zr-based bulk metallic glass. *J. Mater. Res.* **24**(8), 2697 (2009).

32. J.C. Ye, J. Lu, Y. Yang, and P.K. Liaw: Extraction of bulk metallic-glass yield strengths using tapered micropillars in microcompression experiments. *Intermetallics* **18**, 385 (2010).

33. A.C. Fischer Cripps: *Introduction to Contact Mechanics* (Springer, New York, 2000).

34. A. Antoniou, A. Bastarows, and B. Biner: Experimental observations of deformation behavior of bulk metallic glasses during wedge-like cylindrical indentation. *J. Mater. Res.* **22**(2), 514 (2007).

35. F. Yang, D. Li, M.L. Yang, R. Li, W. Jiang, G. Wang, T. Zhang, and P.K. Liaw: Localized deformation of a $Cu_{46.25}Zr_{45.25}Al_{7.5}Er_1$ bulk metallic glass. *J. Phys. D: Appl. Phys.* **42**, 065401 (2009).

36. M. Martin, L. Kecskes, and N.N. Thadhani: Dynamic compression of a zirconium-based bulk metallic glass confined by a stainless steel sleeve. *Scr. Mater.* **59**, 688 (2008).

37. Y. Shi and M.L. Falk: Stress-induced structural transformation and shear banding during simulated nanoindentation of a metallic glass. *Acta Mater.* **55**, 4317 (2007).

38. B.E. Schuster, Q. Wei, T.C. Hufnagel, and K.T. Ramesh: Size-independent strength and deformation mode in compression of a Pd-based metallic glass. *Acta Mater.* **56**, 5091 (2008).

39. B.E. Schuster, Q. Wei, M.H. Ervin, S.O. Hruszkewycz, M.K. Miller, T.C. Hufnagel, and K.T. Ramesh: Bulk and microscale compressive properties of a Pd-based metallic glass. *Scr. Mater.* **57**, 517 (2007).

40. A. Dubach, R. Raghavan, J.F. Loffler, J. Michler, and U. Ramamurty: Micropillar compression studies on a bulk metallic glass in different structural states. *Scr. Mater.* **60**, 567 (2009).

41. C.A. Volkert, A. Donohue, and F. Spaepen: Effect of sample size on deformation in amorphous metals. *J. Appl. Phys.* **103**, 083539 (2008).

42. Y.H. Lai, C.J. Lee, Y.T. Cheng, H.S. Chou, H.M. Chen, X.H. Du, C.I. Chang, J.C. Huang, S.R. Jian, J.S.C. Jang, and T.G. Nieh: Bulk and microscale compressive behavior of a Zr-based metallic glass. *Scr. Mater.* **58**, 890 (2008).

43. C.J. Lee, J.C. Huang, and T.G. Nieh: Sample size effect and microcompression of $Mg_{65}Cu_{25}Gd_{10}$ metallic glass. *Appl. Phys. Lett.* **91**, 161913 (2007).

44. J.S. Harmon, D.M. Demetriou, W.L. Johnson, and K. Samwer: Anelastic to plastic transition in metallic glass-forming liquids. *Phys. Rev. Lett.* **99**, 135502 (2007).

45. J-J. Kim, Y. Choi, S. Suresh, and A.S. Argon: Nanocrystallization during nanoindentation of a bulk amorphous metal alloy at room temperature. *Science* **295**, 654 (2002).

46. K. Wang, T. Fujita, Y.Q. Zeng, N. Nishiyama, A. Inoue, and M.W. Chen: Micromechanisms of serrated flow in a $Ni_{50}Pd_{30}P_{20}$ bulk metallic glass with a large compression plasticity. *Acta Mater.* **56**, 2834 (2008).

47. K. Hajlaoui, A.R. Yavari, B. Doisneau, A. LeMoulec, W.J. Botta, G. Vaughan, A.L. Greer, A. Inoue, W. Zhang, and A. Kvick: Shear delocalization and crack blunting of a metallic glass containing nanoparticles: In situ deformation in TEM analysis. *Scr. Mater.* **54**, 1829 (2006).

48. B.B. Sun, Y.B. Wang, J. Wen, H. Yang, M.L. Sui, J.Q. Wang, and E. Ma: Artifacts induced in metallic glasses during TEM sample preparation. *Scr. Mater.* **53**, 805 (2005).

49. F. Shimizu, S. Ogata, and J. Li: Theory of shear banding in metallic glasses and molecular dynamics calculations. *Mater. Trans., JIM* **48**(11), 2923 (2007).

50. F. Shimizu, S. Ogata, and J. Li: Yield point of metallic glass. *Acta Mater.* **54**, 4293 (2006).

APPENDIX

Under the plane strain condition, the three Hertizian stress components σ_r, σ_z, and τ_{rz}, as defined in Fig. 4(b), can be derived as[33]

$$\sigma_r = -\frac{P_0}{a}\left\{ m\left(1 + \frac{z^2 + n^2}{m^2 + n^2} \right) - 2z \right\} \quad , \qquad \text{(A1)}$$

$$\sigma_z = \frac{P_0}{a} m\left(1 - \frac{z^2 + n^2}{m^2 + n^2} \right) \quad , \qquad \text{(A2)}$$

$$\tau_{rz} = -\frac{P_0}{a} n\left(\frac{m^2 - z^2}{m^2 + n^2} \right) \quad , \qquad \text{(A3)}$$

in which

$$m^2 = \frac{1}{2}[\{(a^2 - r^2 + z^2)^2 + 4r^2z^2\}^{1/2} + (a^2 - r^2 + z^2)] \quad,$$

(A4)

$$n^2 = \frac{1}{2}[\{(a^2 - r^2 + z^2)^2 + 4r^2z^2\}^{1/2} - (a^2 - r^2 + z^2)] \quad,$$

(A5)

$$P_0 = \left(\frac{PE^*}{\pi R}\right)^{1/2} \quad,$$

(A6)

where a is the contact diameter; r is the radial distance to the axis of symmetry; z is the distance to the sample surface; R is the indenter tip radius; P is the indentation load and E^* is the reduced modulus and defined as

$$\frac{1}{E^*} = \frac{1 - v^2}{E} + \frac{1 - v_i^2}{E_i} \quad.$$

(A7)

In Eq. (A7), E and E_i denote, respectively, the Young's moduli of the BMG and the diamond indenter; whereas v and v_i denote the Poisson's ratios of the BMG and the diamond indenter, respectively.

J. Mater. Res., Vol. 25, No. 3, Mar 2010

575